J. Fluid Mech. (2008), *vol.* 596, *pp.* 437–466.
doi:10.1017/S0022112007009688 Printed in the United Kingdom

Numerical investigation of particle–particle and particle–wall collisions in a viscous fluid

A. M. ARDEKANI AND R. H. RANGEL

Department of Mechanical and Aerospace Engineering, University of California, Irvine, CA 92697-3975, USA

(Received 2 February 2007 and in revised form 23 October 2007)

The dynamics of particle–particle collisions and the bouncing motion of a particle colliding with a wall in a viscous fluid is numerically investigated. The dependence of the effective coefficient of restitution on the Stokes number and surface roughness is analysed. A distributed Lagrange multiplier-based computational method in a solid–fluid system is developed and an efficient method for predicting the collision between particles is presented. A comparison between this method and previous collision strategies shows that the present approach has some significant advantages over them. Comparison of the present methodology with experimental studies for the bouncing motion of a spherical particle onto a wall shows very good agreement and validates the collision model. Finally, the effect of the coefficient of restitution for a dry collision on the vortex dynamics associated with this problem is discussed.

1. Introduction

Collisions between particles in a dispersed flow occur in several natural and industrial applications such as sedimentation, crystal growth, and microfluidic devices. For example, the design and utilization of microfluidic devices for mechanical cell lysis requires a better understanding of particle collisions in low and intermediate Reynolds number flows.

To accurately predict the behaviour of particulate flows, fundamental knowledge of the mechanisms of particle–particle and particle–wall interactions is required. Most of the existing theoretical studies focus on particle interaction at low Reynolds numbers. Classical lubrication theory predicts that the lubrication force is singular as the distance between two smooth spheres approaches zero and hence prevents smooth spheres from touching. In practice, no general numerical method can afford the computational cost of resolving the flow in the narrow gaps between closely spaced particles and some modelling is needed. On the other hand, experiments have shown that for rough particles, physical contact could occur which would affect the relative motion of the particles (Arp & Mason 1977).

Kushch *et al.* (2002) developed a viscous potential flow model for the motion of high-Reynolds-number and finite-Weber-number bubbly flows. They showed that the use of the potential flow approximation together with non-hydrodynamic repulsive forces from an image bubble for the collision of a rising bubble with a horizontal wall yields good agreement with the experimental results by Tsao & Koch (1994). However, the mechanism for the bouncing phenomenon may be different from the one modelled, since the interaction of the viscous boundary layer at the wall with the bubble is not taken into account.

Davis (1992) considered a roll/slip model and a stick/rotate model for the motion of touching spheres in Stokes flow and found that the roll/slip model is consistent with experiments (Zeng, Kerns & Davis 1996). Ekiel-Jezewska *et al.* (1999, 2002) used the roll/slip model of contact for interaction between two spherical particles immersed in a viscous fluid. Comparison of the model with experimental results for the settling motion of a sphere in the vicinity of another fixed sphere showed good agreement.

Zhang *et al.* (1999) considered collision of a sphere onto a stationary sphere at finite Reynolds numbers. Their experimental results are in agreement with the mechanistic model they developed and the numerical results using the lattice Boltzmann method. Lin, Wang & Olsen (2004) studied an elastic collision between two cylindrical particles also using the lattice Boltzmann method.

Particulate flow simulations under the Stokes flow assumption have been conducted using Stokesian dynamics techniques (Brady & Bossis 1988). For dilute suspensions, the unsteady motion of two solid spheres has also been analysed (Ardekani & Rangel 2006). However, for intermediate Reynolds numbers the use of numerical simulation is generally unavoidable. A distributed Lagrange multiplier (DLM)-based computational method is used here in order to simulate particulate flow and collisions between particles. The DLM method, developed in the last decade for direct simulations of particulate flow, was presented by Glowinski *et al.* (1998, 1999), who employed a finite-element method with a fixed structured grid, thus eliminating the need for remeshing required for unstructured boundary-fitted grids. In this method, the entire domain is treated as a fluid, but the fluid inside the particle domain satisfies a rigidity constraint by using Lagrange multipliers. The DLM solution can be formulated by forcing the deformation tensor in the particle domain to be zero, thus eliminating $\boldsymbol{U}$ and $\boldsymbol{\omega}$ as variables from the coupled system of equations, where $\boldsymbol{U}$ and $\boldsymbol{\omega}$ are the translational and angular velocity of the particle, respectively (Patankar *et al.* 2000; Patankar 2001). This formulation introduces a stress field in the particle domain similar to the pressure in an incompressible fluid. Sharma, Chen & Patankar (2005) presented a formulation based on DLM for steady Stokes flow using a control volume method. Similarly, a numerical simulation developed in the present paper is based on the DLM approach implemented using a control volume method and the SIMPLE (Patankar 1980) algorithm.

In practice, for a particulate system with a large number of particles, no general numerical method can afford the computational cost of resolving the flow in the narrow gaps between closely spaced particles. Therefore, using lubrication theory becomes necessary. In lattice Boltzmann simulations (LADD 1994*a*, *b*) or Stokes multipole simulations (Brady & Bossis 1988; Sangani & Mo 1994), lubrication forces are incorporated when the particles are near contact. Similarly, lubrication forces can be applied to the particles instead of refining the grid between neighbouring particles utilizing the DLM method.

Previous analyses show that smooth particles do not come into physical contact under finite forces (Davis 1987). However, in numerical simulations, contact can occur due to numerical truncation errors and thus it is necessary to use a reliable collision strategy. In earlier approaches, a repulsive force was applied to the particles when their separation was less than a critical value. In order to have at most one rigid-body motion constraint at each node, the particles were limited to be more than one grid element apart, as described by Glowinski *et al.* (1999) and Singh *et al.* (2000). Singh, Hesla & Joseph (2003) modified DLM in order to eliminate the so-called security zone by allowing the particles to be close to each other and even overlap. They used

the constraint of the closer particle to the node, in order to prevent the conflict of having two rigid-body constraints at one node. The repulsive force is applied when the particles overlap. In these collision schemes, the choice of the stiffness parameter is important. If the stiffness parameter is too small, the collision will not be prevented, and if it is too large, the repulsive force will be too strong and particles will bounce unrealistically, as explained by Hu, Patankar & Zhu (2001). Another approach is to use the solid-body collision model which neglects the fluid during the collision process. In this method, a fully explicit scheme is used for updating particle positions and velocities but the method can be unstable, as noted by Hu *et al.* (2001).

In this paper, we do not apply a repulsive force and instead the contact force between particles is computed. By using conservation of linear momentum along the particles line of centres, both particles can be rigidified together. One advantage of this method is that the particle velocity is not updated explicitly, thus preventing numerical instabilities. Furthermore, unlike in earlier approaches, there is no possibility of having two constraints for one node. Contact starts when the distance between particles becomes zero for smooth particles and ends when the contact force becomes zero or negative since the particles cannot apply a tensile force to each other. For particles with surface roughness, the contact starts when their separation reaches the roughness height.

In reality the particles possess some elasticity and the fluid has some compressibility so that the instantaneous change in the particle velocity results in a continuous change in the fluid velocity and pressure fields. Here we assume that the particle is rigid and the fluid is incompressible. Thus, the instantaneous change in particle velocity leads to an instantaneous change in the velocity field due to the elliptic nature of the governing equations. Integrating the Navier–Stokes equation during the collision processes, we have

$$\rho_f \{\boldsymbol{u}(t_c^+) - \boldsymbol{u}(t_c^-)\} = -\nabla \tilde{I}, \tag{1.1}$$

where $\tilde{I}$ is the pressure impulse, t_c is the time at which the collision occurs. Superscripts $-$ and $+$ refer to infinitesimal times before and after the collision, respectively. Thus, the pressure gradient will be unbounded and numerically we obtain a finite pressure impulse.

There are several studies on the rebound of colliding particles in recent years. Davis, Serayssol & Hinch (1986) employed an elastohydrodynamic model for collision between particles suspended in a liquid. Throughout these collisions, the particles are separated by a viscous liquid film. The pressure force in this lubrication film is sufficiently large to cause the particles to deform and rebound without making solid-body contact. They showed that the pertinent parameter for collision in the fluid is not the Reynolds number Re but the Stokes number $St = \frac{1}{9}(\rho_p/\rho_f)Re$, where ρ_p and ρ_f are the particle and fluid densities, respectively. No rebound occurs for St lower than a critical value due to the fact that the elastic energy stored by the particle deformation is dissipated in the fluid. The experiments by Joseph *et al.* (2001) show that the rebound velocity depends strongly on the impact Stokes number and weakly on the elastic properties of the material, where the Stokes number is defined using the approaching velocity of the particles. It has been shown that below a St of 10, no rebound occurs (e.g. Joseph *et al.* 2001; Gondret *et al.* 1999, 2002). For impact Stokes numbers larger than 500 the coefficient of restitution asymptotes to that for a dry collision. Davis *et al.* (1986) concluded that the Stokes number dependence is due to the drainage of the liquid film formed between the particle and the wall, as

noted by Legendre *et al.* (2006). Barnocky & Davis (1989) considered the variation of the density and viscosity with pressure. The increase in viscosity and density with pressure leads to solidification of the fluid in the contact region and affects the rebound. However, they concluded that the effect of the increase in viscosity on the normal collision behaviour is small (noted by Joseph & Hunt 2004).

Surface roughness has a significant effect on rebound velocity because the lubrication layer between two colliding objects is very small, and may be of the same order of magnitude as the surface roughness, and consequently, contact may occur through microscopic surface imperfections, as noted by Smart & Leighton (1989). Davis (1987) developed a theory for the collision of rough surfaces with small bumps with dilute surface coverage. He showed that the surface roughness has negligible effect on the viscous force until the gap between the smooth surfaces becomes equal to the size of largest roughness element. At this time, the bumps make physical contact due to the discrete molecular nature of the fluid and/or attractive London–van der Waals forces, further approach is prevented, and solid–solid contact occurs.

Whereas several experimental studies have been conducted on the influence of the fluid on the collision process, few numerical studies address this issue. In this work, we numerically study the effects of surface roughness and Stokes number on the rebound velocity and obtain results which are in agreement with the experimental results by Gondret *et al.* (2002). The governing equations are presented in § 2. A simple and efficient computational scheme is described in § 3. The collision strategy is explained in § 4. Finally, the method is verified by applying it to different fluid–particle interaction problems in § 5. Bouncing motion of a spherical particle towards a wall is studied numerically and the results are compared with experimental results.

2. Theoretical development

In this section, the DLM method for the motion of one particle is described but the method can be easily extended for additional particles. Let Γ represent the fluid boundary which is not shared with the particle. The solid domain and its boundary are denoted by P and ∂P, respectively. The computational domain is Ω, including both the fluid and the particle. The governing equations in the fluid domain are

$$\rho_f \frac{\mathrm{D}\boldsymbol{u}}{\mathrm{D}t} = \nabla\cdot\boldsymbol{\sigma} + \rho_f\ \boldsymbol{g} \quad \text{in } \Omega \setminus \overline{P}, \tag{2.1}$$

$$\nabla\cdot\boldsymbol{u} = 0 \quad \text{in } \Omega \setminus \overline{P}, \tag{2.2}$$

$$\boldsymbol{u} = \boldsymbol{U}_i \text{ on } \partial P, \tag{2.3}$$

$$\boldsymbol{\sigma}\cdot\boldsymbol{n} = \boldsymbol{t} \quad \text{on } \partial P, \tag{2.4}$$

$$\boldsymbol{u}|_{t=0} = \boldsymbol{u}_0(\boldsymbol{x}) \text{ in } \Omega \setminus \overline{P}, \tag{2.5}$$

in addition to the outer boundary conditions on Γ. In these equations, $\boldsymbol{u}$ is the fluid velocity, $\boldsymbol{g}$ is the acceleration of gravity, ρ_f is the fluid density, $\boldsymbol{n}$ is the normal unit vector, $\boldsymbol{U}_i$ is the particle velocity, and $\boldsymbol{t}$ is the traction vector on the particle surface. The initial velocity $\boldsymbol{u}_0$ satisfies the continuity equation, $\boldsymbol{\sigma} = -p\boldsymbol{I} + \boldsymbol{\tau}$ is the stress tensor, p is the pressure field, $\boldsymbol{I}$ is the identity tensor, and $\boldsymbol{\tau}$ is the viscous stress:

$$\boldsymbol{\tau} = 2\mu\boldsymbol{D}[\boldsymbol{u}] = \mu[\nabla\boldsymbol{u} + (\nabla\boldsymbol{u})^T]. \tag{2.6}$$

The governing equations in the particle domain are

$$\rho_P \frac{\mathrm{D}\boldsymbol{u}}{\mathrm{D}t} = \nabla\cdot\boldsymbol{\sigma} + \rho_P \boldsymbol{g} \quad \text{in } P, \tag{2.7}$$

$$\nabla\cdot\boldsymbol{u} = 0 \quad \text{in } P, \tag{2.8}$$

$$\boldsymbol{D}[\boldsymbol{u}] = 0 \quad \text{in } P, \tag{2.9}$$

$$\boldsymbol{u} = \boldsymbol{U}_i \quad \text{on } \partial P, \tag{2.10}$$

$$\boldsymbol{\sigma}\cdot\boldsymbol{n} = \boldsymbol{t} \quad \text{on } \partial P, \tag{2.11}$$

$$\boldsymbol{u}|_{t=0} = \boldsymbol{u}_0(\boldsymbol{x}) \quad \text{in } P, \tag{2.12}$$

where ρ_P is the particle density. Equation (2.9) satisfies the continuity equation, but in order to facilitate numerical implementation, equation (2.8) is retained. As pointed out by Sharma *et al.* (2005), the rigidity constraint gives rise to a stress field inside the particle which is a function of three scalar Lagrange multipliers for three-dimensional problems. Thus, for a two-dimensional problem, the stress field can be represented in terms of two scalars:

$$\boldsymbol{\sigma} = -p\boldsymbol{I} + \boldsymbol{\tau} + \boldsymbol{D}[\lambda], \tag{2.13}$$

where $\boldsymbol{\lambda}$ represents the Lagrange multipliers and $\boldsymbol{\tau}$ is zero inside the particle due to the rigidity constraint. The governing equations in the entire domain can be combined as

$$\rho\frac{D\boldsymbol{u}}{Dt} = \nabla\cdot\boldsymbol{\sigma} + \rho\boldsymbol{g} + \boldsymbol{f} \quad \text{in } \Omega, \tag{2.14}$$

$$\nabla\cdot\boldsymbol{u} = 0 \quad \text{in } \Omega, \tag{2.15}$$

$$\boldsymbol{u}|_{t=0} = \boldsymbol{u}_0(\boldsymbol{x}) \quad \text{in } \Omega, \tag{2.16}$$

where

$$\rho = \begin{cases} \rho_f & \text{in } \Omega \setminus \overline{P}, \\ \rho_P & \text{in } P, \end{cases} \tag{2.17}$$

in addition to the outer boundary conditions on Γ. In the above equations, $\boldsymbol{f} = \nabla\cdot\boldsymbol{D}[\boldsymbol{\lambda}]$ is zero everywhere except in the particle domain and leads to the rigid-body motion inside the particle.

3. Numerical implementation

A finite-volume method using a staggered grid for incompressible flow is implemented. The SIMPLE algorithm (Patankar 1980) is used to solve the fluid equations with modifications to account for the presence of particles. The Crank–Nicolson scheme is used for time discretization.

The discretized momentum equations in the x and y directions are

$$a_{i,J}u_{i,J} = \sum a_{nb}u_{nb} - \frac{p_{I,J} - p_{I-1,J}}{\delta x_u}\Delta V_u + b_{i,J} + F_x, \tag{3.1}$$

$$a_{I,j}v_{I,j} = \sum a_{nb}v_{nb} - \frac{p_{I,J} - p_{I,J-1}}{\delta x_v}\Delta V_v + b_{I,j} + F_y, \tag{3.2}$$

where ΔV_u and ΔV_v are the volumes of the u-cell and v-cell, respectively; u and v represent the horizontal and vertical components of the velocity field; I and J are the nodes at the centre of the main control volumes; while i and j represent the nodes

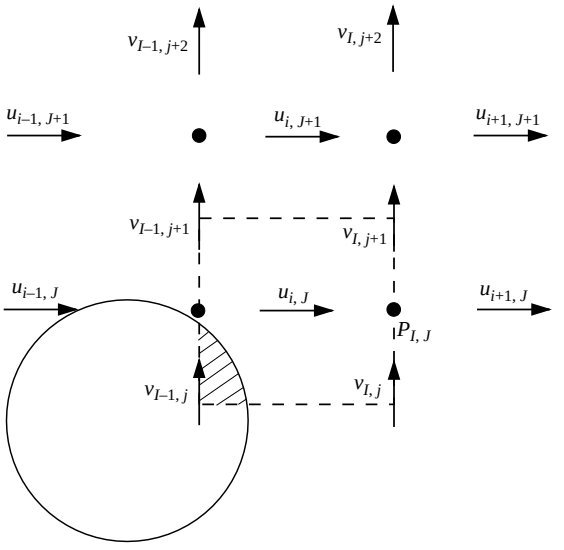

FIGURE 1. Staggered grid, u control volume and corresponding volume fraction.

at the centre of the control volumes for u and v, respectively, as shown in figure 1. Subscript nb refers to corresponding neighbouring staggered control volumes; b is the momentum source term which includes the gravity term; and $\boldsymbol{F}$ represents the rigidity force which makes the velocity field inside the particle domain satisfy the rigidity constraint.

Following the SIMPLE algorithm and taking the particles into account, the force $\boldsymbol{F}$ is added as an unknown variable, and $\boldsymbol{F} = \boldsymbol{F}^* + \boldsymbol{F}'$, where $\boldsymbol{F}^*$ is the force predicted at each iteration (the force calculated in the previous iteration), and $\boldsymbol{F}'$ is the correction force. At each iteration, the rigidity force is defined as

$$F_{xi,J} = F^*_{xi,J} + C\rho_P A_{i,J}(u_{i,J} - u_{Ri,J}), \tag{3.3}$$

and similarly, in the y direction,

$$F_{yI,j} = F^*_{yI,j} + C\rho_P A_{I,j}(v_{I,j} - v_{RI,j}), \tag{3.4}$$

where C is a dimensional constant; $A_{i,J}$ and $A_{I,j}$ are the areas of the u-cell and v-cell, respectively; while $\boldsymbol{u}_R$ is the velocity vector rigidified inside the particle, equal to $\boldsymbol{u}$ outside the particle domain, and defined as follows:

$$\boldsymbol{u}_R = (1-\phi)\boldsymbol{u} + \phi\boldsymbol{u}_P, \tag{3.5}$$

where ϕ is the volume fraction occupied by the particle in each control volume, defined separately for u- and v-cells. For example, as shown in figure 1, $\phi_u = \Delta V_{hatched}/\Delta V_u$. In the present study, ϕ is exactly calculated while $\boldsymbol{u}_P$, defined only in the particle domain, can be calculated as follows:

$$\boldsymbol{u}_P = \boldsymbol{U}_P + \boldsymbol{\omega} \times \boldsymbol{r}, \tag{3.6}$$

where $\boldsymbol{U}_P$ and $\boldsymbol{\omega}$ are the particle translational and angular velocities. By using conservation of linear and angular momentum for the solid particle, one can calculate the particle translational and angular velocities as follows (Sharma *et al.* 2005;

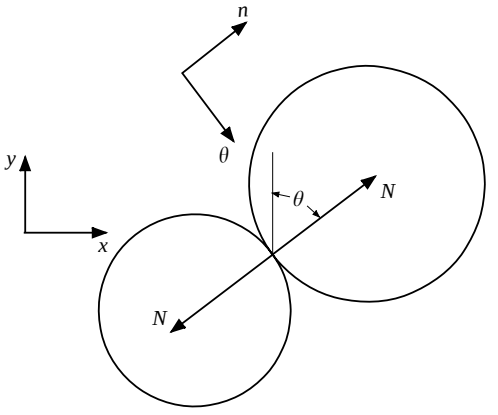

FIGURE 2. Schematic of problem and coordinate systems.

Sharma & Patankar 2005):

$$M_P \boldsymbol{U}_P = \int_P \rho \boldsymbol{u} \, \mathrm{d}\boldsymbol{x} \quad \text{and } \boldsymbol{I}_P \boldsymbol{\omega} = \int_P \boldsymbol{r} \times \rho \boldsymbol{u} \, \mathrm{d}\boldsymbol{x}. \tag{3.7}$$

Defining a rigidity force as in equations (3.3) and (3.4) guarantees that, upon convergence at each time step, $\boldsymbol{u} = \boldsymbol{u}_R$ everywhere in the entire domain. The summation of $\boldsymbol{F}$ over each particle is equal to the external forces applied to that particle, excluding the gravitational and hydrodynamic forces since these two forces are included in equation (2.7). Thus, when particles are not in contact we have

$$\sum_i \sum_J F_{xi,J} = \sum_I \sum_j F_{yI,j} = 0. \tag{3.8}$$

Using (3.3) and (3.4) guarantees that the total rigidity force applied to each particle is zero at each iteration. Finally, the modifications due to the presence of the particle can be included by adding $\boldsymbol{F}$ as a source term in the momentum equations. Equations (3.3) and (3.4) are solved after the pressure correction step.

4. Collision strategy

Now, we consider the collision between two particles when the dry coefficient of restitution is zero. For a frictionless collision, the tangential force is zero and the same normal force applies to each particle in opposite directions, as shown in figure 2.

Thus, during the collision process, instead of enforcing conservation of linear momentum for each particle separately, as is done in deriving equation (3.7), linear momentum will be conserved for the system of both particles along their line of centres. Meanwhile, linear momentum is conserved in the tangential direction separately for each particle. The collision process in this method starts when the distance between particles is zero for smooth particles or equal to the roughness height ($h_{\min}$) for particles with a rough surface. We assume that rough surfaces have small bumps with dilute surface coverage and have negligible effect on the viscous force until the gap between the smooth portions of surfaces becomes equal to the size of largest roughness element. The contact ends when the normal force becomes equal to or less than zero, since the particles cannot apply a tensile force to each other.

Using the preceding concepts during the collision process, we write

$$U_{nP1} = U_{nP2} = \frac{\int_{P1,P2} \rho u_n \, \mathrm{d}\boldsymbol{x}}{M_{total}}, \tag{4.1}$$

$$U_{\theta P_\alpha} = \frac{\int_{P_\alpha} \rho u_\theta \, \mathrm{d}\boldsymbol{x}}{M_{P_\alpha}}, \tag{4.2}$$

$$\boldsymbol{\omega}_{P_\alpha} = \frac{\int_{P_\alpha} \boldsymbol{r} \times \rho \boldsymbol{u} \, \mathrm{d}\boldsymbol{x}}{\boldsymbol{I}_{P_\alpha}}, \tag{4.3}$$

$$U_{P_\alpha} = U_{nP_\alpha} \sin\theta + U_{\theta P_\alpha} \cos\theta, \tag{4.4}$$

$$V_{P_\alpha} = U_{nP_\alpha} \cos\theta - U_{\theta P_\alpha} \sin\theta, \tag{4.5}$$

$$N = \sum_i \sum_J F_{xi,J} \sin\theta + \sum_I \sum_j F_{yI,j} \cos\theta, \tag{4.6}$$

where u_n is the normal velocity, u_θ is the tangential velocity, N represents the normal force applied to each particle, and α is the particle index (1 or 2). In earlier methods, a repulsive force function of distance between particles, was used. These methods do not guarantee that the particles will not overlap and the minimum distance between particles and the rebound velocity depend strongly on a stiffness parameter. In the present method, we can calculate the contact force between particles, and this is used as a criterion to determine the end of the collision process and no other repulsive force is employed.

The experimental data by Joseph *et al.* (2001) demonstrate that below a Stokes number of 10, no rebound occurs, while for impact Stokes numbers above 500, the coefficient of restitution appears to asymptote to the coefficient of restitution for a dry collision e_{dc}. Now, we introduce a strategy to handle collision for cases where rebound occurs. Due to the conservation of linear momentum for the system of two particles along their line of centres, we have

$$M_{P1} U_{nP1}^{t_c^+} + M_{P2} U_{nP2}^{t_c^+} = \int_{P1,P2} \rho u_n \, \mathrm{d}\boldsymbol{x}, \tag{4.7}$$

where t_c is the time at which the collision starts (distance between particles becomes equal to $h_{\min}$). Superscripts $-$ and $+$ refer to infinitesimal times before and after the collision, respectively. Using the definition of the dry coefficient of restitution, we write

$$U_{nP2}^{t_c^+} - U_{nP1}^{t_c^+} = -e_{dc}\left(U_{nP2}^{t_c^-} - U_{nP1}^{t_c^-}\right), \tag{4.8}$$

where e is the coefficient of restitution. Solving for $U_{nP2}^{t_c^+}$ and $U_{nP1}^{t_c^+}$ by using equation (4.7) and (4.8), we have

$$U_{nP1}^{t_c^+} = \frac{e_{dc}\left(U_{nP2}^{t_c^-} - U_{nP1}^{t_c^-}\right) M_{P2}}{M_{P1} + M_{P2}} + \frac{\int_{P1,P2} \rho u_n \, \mathrm{d}\boldsymbol{x}}{M_{total}}, \tag{4.9}$$

$$U_{nP2}^{t_c^+} = -\frac{e_{dc}\left(U_{nP2}^{t_c^-} - U_{nP1}^{t_c^-}\right) M_{P1}}{M_{P1} + M_{P2}} + \frac{\int_{P1,P2} \rho u_n \, \mathrm{d}\boldsymbol{x}}{M_{total}}. \tag{4.10}$$

Equation (4.1) is a special case of equations (4.9) and (4.10) with $e_{dc} = 0$, i.e. plastic collision. As explained earlier, linear momentum in the tangential direction and angular velocity are conserved for each particle separately. Thus, by using the following equations, the particle linear and angular velocities can be calculated:

$$U_{\theta P_\alpha} = \frac{\int_{P_\alpha} \rho u_\theta \, \mathrm{d}\boldsymbol{x}}{M_{P_\alpha}}, \tag{4.11}$$

$$\boldsymbol{\omega}_{P_\alpha} = \frac{\int_{P_\alpha} \boldsymbol{r} \times \rho \boldsymbol{u} \, \mathrm{d}\boldsymbol{x}}{\boldsymbol{I}_{P_\alpha}}, \tag{4.12}$$

$$U_{P_\alpha} = U_{nP_\alpha} \sin\theta + U_{\theta P_\alpha} \cos\theta, \tag{4.13}$$

$$V_{P_\alpha} = U_{nP_\alpha} \cos\theta - U_{\theta P_\alpha} \sin\theta. \tag{4.14}$$

This approach can be extended to particulate flow with large number of particles, and the extension of the method to objects of general shape needs further investigation. In extending this method to turbulent flow situations, it is noteworthy that the kinetic energy is lost during the collision process and this can affect the computational calculations of the energy cascade.

5. Results and discussion

5.1. *Sedimentation of a circular particle in a two-dimensional channel*

In this section, results for the fluid–particle solver without collisions are compared with available results. We first conduct a simulation for sedimentation of a circular cylinder in a two-dimensional channel. We compare the present results with results presented by Feng, Hu & Joseph (1994). A circular particle with a diameter d is released in a vertical channel with a width $W = 1.5d$ under gravity where $g = 981\,\mathrm{cm\,s^{-2}}$. The initial linear and angular velocities of the particle are zero. The solid-to-liquid density ratio is 1.3 and the Reynolds number based on particle diameter and particle terminal velocity is 6.28. A moving computational domain is used in order to simulate an infinite channel. The upstream boundary of the computational domain is $10d$ upstream of the particle, whereas the downstream boundary is $15d$ from the particle. The normal derivative of velocity is zero at the downstream boundary and the vertical walls move with the average vertical velocity of the particle. In the present simulation, the fluid density ρ_f is 1, the particle diameter is 0.5, the fluid viscosity μ is 0.1157, and $y_0 = 0.6d$, where y_0 is the initial horizontal position of the particle centre. All dimensional quantities in this paper are in the CGS system unless otherwise stated. 100×570 nodes are used, the smallest mesh size is 0.0075×0.0075, and the time step is 0.004. Figure 3 compares present results with the results by Feng *et al.* As can be seen, our results are in good agreement with the published results. The particle moves away from the wall and oscillates about the channel centreline until it reaches equilibrium and moves along the centreline.

5.2. *Sedimentation of two circular particles in a two-dimensional channel filled with a Newtonian fluid*

In this section, we present the sedimentation of two circular particles in a Newtonian fluid inside the vertical channel. The conditions used here are equal to those used by Glowinski *et al.* (1999). The fluid density is $\rho_f = 1$, the acceleration of gravity is $g = 981$, the viscosity is $\mu = 0.01$, the particle diameters are 0.25 and the solid-to-fluid

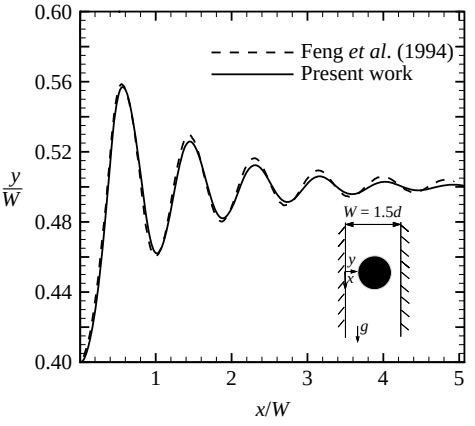

FIGURE 3. Trajectory of settling particle in a vertical channel. $Re = 6.28$ and $\rho_p/\rho_f = 1.3$.

density ratio is 1.5. Particles are released from rest in a channel with a width of 2 and a height of 5. The particles are initially at the centre of the channel at $y = 1.5$ and $y = 2$. The Reynolds number based on the maximum velocity of the particles is 470.

The lubrication force acting on two cylinders is linearly proportional to $h^{-3/2}$, and hence the cylinders do not touch in finite time. However, in a numerical simulation, an infinitesimal grid spacing is necessary to prevent contact, which is not computationally affordable. One could use lubrication theory when the cylinders are sufficiently close to obtain an approximate solution. In the simulations presented here, the cylinders are not smooth but have a roughness of $h_{\min} = 0.01\,\%d$.

A moving computational domain is used and the boundary conditions are the same as the previous case. We present results for two different mesh sizes of 0.01 and 0.0066 and two different time steps of 0.001 and 0.0005. Figures 4 and 5 indicate that the motion of the particles is independent of mesh size and time step before collision. As will be shown at the end of this section, the post-collision trajectories of particles are highly sensitive to small variations in the trajectories before collision and consequently can change significantly with mesh size and time step. This type of chaotic behaviour was noted by Singh *et al.* (2003), who considered it impractical to refine the time step and mesh size to accurately capture the post-collision trajectories. However, as will be shown later, the separation time is strongly affected by those small variations in the pre-collision trajectories but the post-collision behaviour of the particles is almost unchanged and it is only shifted in time.

Figure 6 shows the agreement between the present results and the results by Glowinski *et al.* (1999) for the pre-collision behaviour of the particles. In this example, the coefficient of restitution for a dry collision is assumed to be zero and therefore, even though the impact Stokes number is about 18, no rebound occurs. The cases with non-zero coefficient of restitution are presented in the next section.

We now consider the effect of surface roughness. Experimental results by Smart & Leighton (1989) show that the manufacturing processes generate microscopic roughness elements on the particle surface, which are typically of order 10^{-3} to 10^{-2} times the particle radius. The density of these asperities was sufficiently large to prevent smooth sections of the surface contacting each other but sufficiently sparse not to interfere with the fluid in the gap between the two surfaces. Figure 7 compares the results for particles with different surface roughness. It can be seen that the

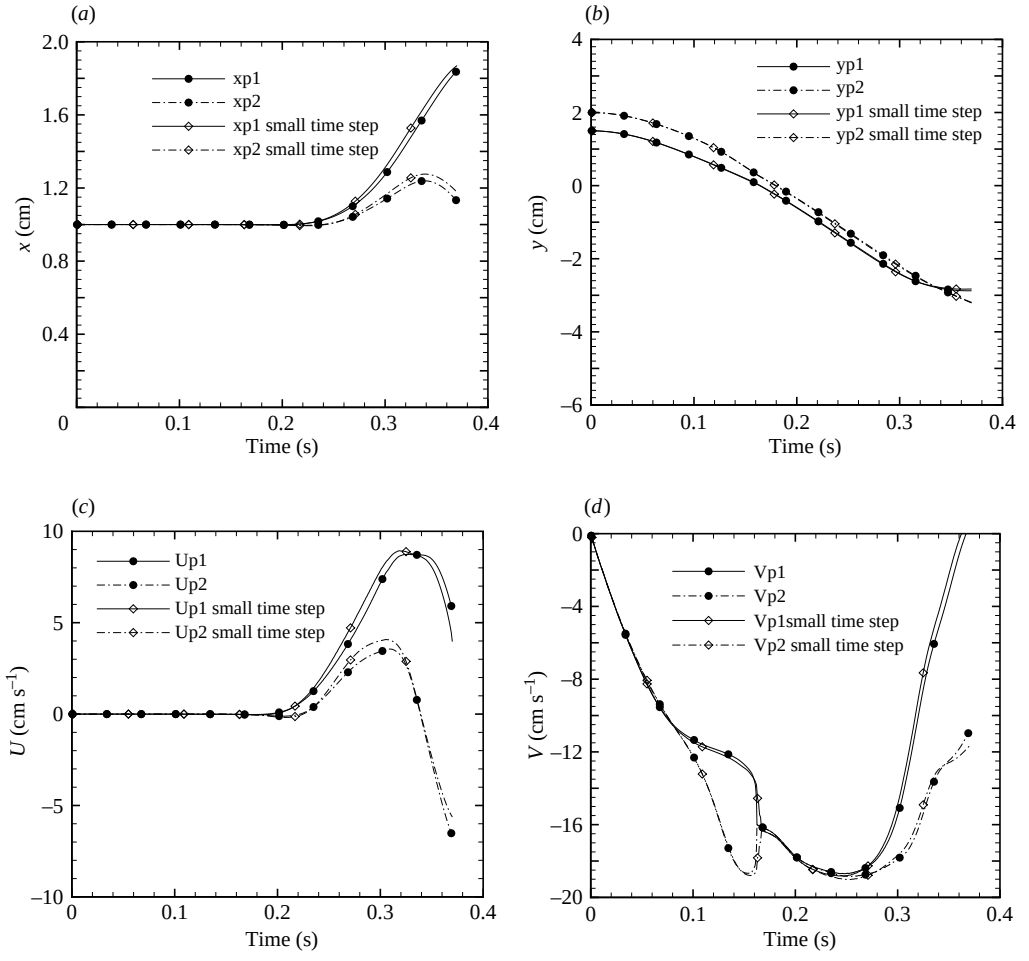

FIGURE 4. Sedimentation of two circular particles. Particle position and velocity for two cases are compared. The first case (•) has a mesh size of 0.01 and a time step of 0.001. In the second case (◇), the mesh size is 0.01 and the time step is 0.0005. (*a*) Horizontal position, (*b*) vertical position, (*c*) *u* velocity, (*d*) *v* velocity.

only effect of increasing the surface roughness is that collision occurs earlier but the post-collision behaviour is almost unchanged.

Figure 8 shows the normal force N applied to particle 2. As can be seen, this force is zero when the particles are not in contact, increases rapidly and then decreases until it becomes zero and the particles separate. After this time N remains equal to zero.

We now consider a lower Reynolds number flow. The conditions used here are equal to those in the problem solved by Singh *et al.* (2003) except that a moving computational domain is used here (the results presented by Singh *et al.* 2003 are for $\mu = 0.05$, although reported incorrectly as $\mu = 0.08$). The boundary conditions are the same as in the previous cases. The fluid density is $\rho_f = 1$, the acceleration of gravity is $g = 981$, the viscosity is $\mu = 0.08$, the particle diameters are 0.2, and the solid-to-fluid density ratio is 1.1. The particles are released from rest in a channel with a width of 2 and a height of 6. The particles are initially at the centre of the

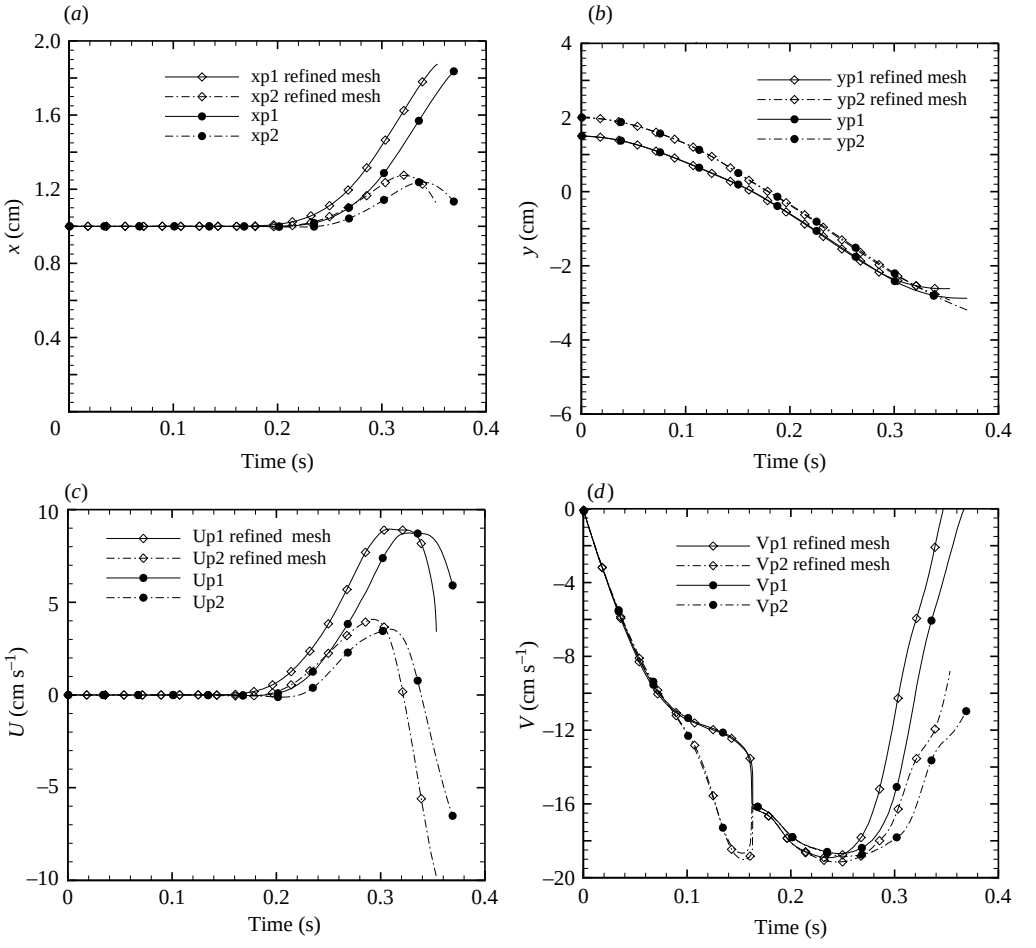

FIGURE 5. Sedimentation of two circular particles. Particle position and velocity for two cases are compared. The first case (●) has a mesh size of 0.0066 and a time step of 0.00033. In the second case (◇), the mesh size is 0.01 and the time step is 0.001. (*a*) Horizontal position, (*b*) vertical position, (*c*) u velocity, (*d*) v velocity.

channel and their separation distance is 0.3. The Reynolds number based on the maximum velocity is about 10 and the impact Stokes number of the particles is about 0.3; thus no rebound occurs. Figure 9 shows a comparison with the results of Singh *et al.* (2003). No repulsive force is used in the present collision strategy which results in larger separation time. The separation time in our calculations is larger than the one obtained by Singh *et al.* (2003), while their results predict larger separation times than those produced by Glowinski *et al.* (1999). Numerical tests were conducted to show that the motion of the particles is independent of mesh size and time step before collision. The effect of surface roughness is shown in figure 10. It can be seen that collision and separation start earlier but the particle velocities after separation remain similar. Figure 11 compares results for two different initial conditions. In the first case, the particles are located along the channel centreline. In the second case, the upper particle is moved to the right a distance of 0.5 % of the particle diameter. As can be observed, the separation time is strongly affected by this disturbance in the system but the post-collision behaviour of the particles is unchanged.

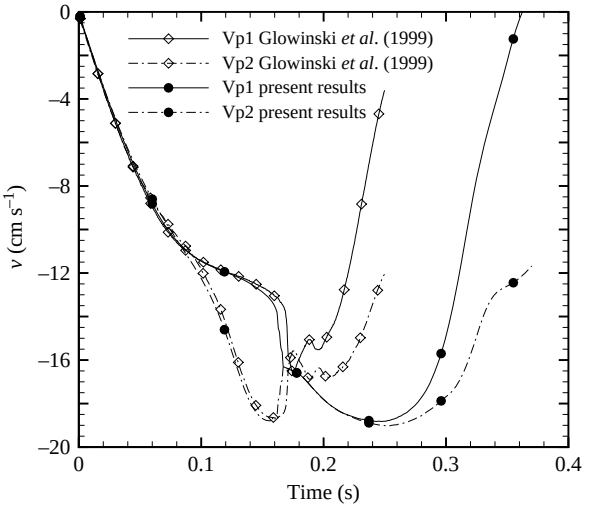

FIGURE 6. Sedimentation of two circular particles. Comparison of present results and results by Glowinski *et al.* (1999) for particle vertical velocity. In our results the mesh size is 0.01 and the time step is 0.0005.

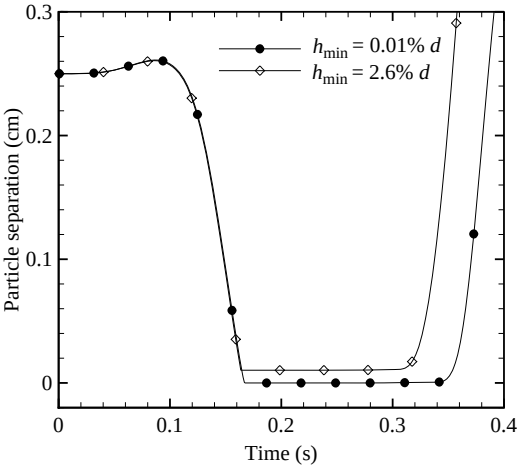

FIGURE 7. Sedimentation of two circular particles. In the first case (•) the roughness height is 0.01% of the particle diameter and in the second case (◇) it is 2.6% of the particle diameter. The mesh size is 0.0066 and the time step is 0.00066. The Reynolds number based on the maximum velocity of the particles is 470.

5.3. *Sedimentation of a spherical particle towards a wall*

In the previous cases, the dry coefficient of restitution is assumed to be zero and thus no rebound is observed. In this section, we examine the motion of a spherical particle which is moving towards a wall with a non-zero dry coefficient of restitution. Specifically, the collision of a steel sphere with density of 7.8 with a glass wall is investigated. The dry coefficient of restitution for this system is equal to 0.97 ± 0.02 according to the data reported by Gondret *et al.* (2002). The sphere is moving in oil with density of 0.935 and viscosity of 0.1. The sphere diameter is 0.3 and the gravitational acceleration is $g = 981$. The numerical simulation is performed

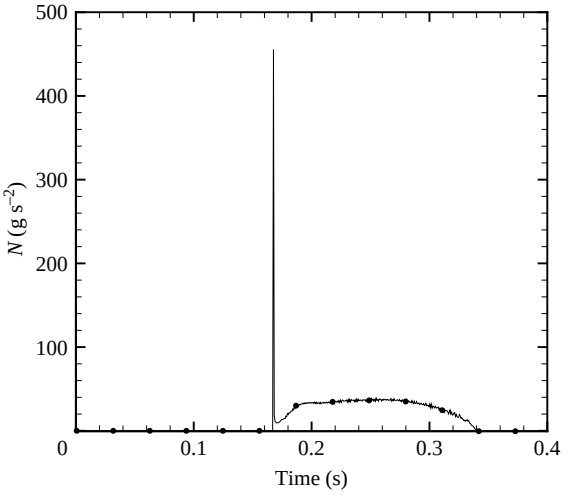

FIGURE 8. Normal force applied to particle 2. The mesh size is 0.0066 and the time step is 0.00066. The Reynolds number based on the maximum velocity of the particles is 470.

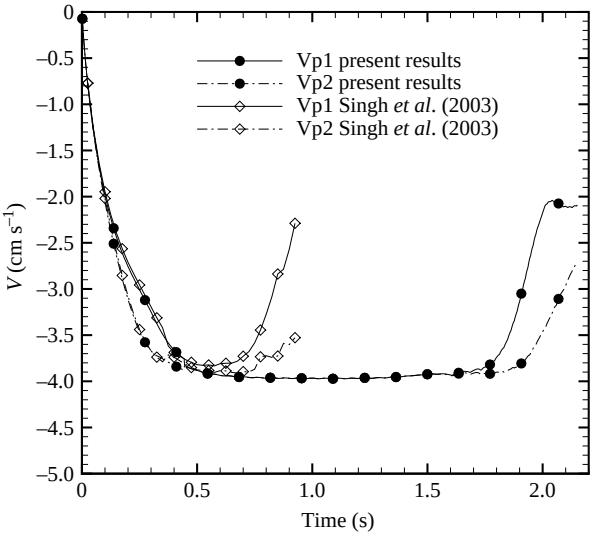

FIGURE 9. Sedimentation of two circular particles. Comparison of present results and results by Singh *et al.* (2003) for particle vertical velocity. In our results the mesh size is 0.014 and the time step is 0.0035.

utilizing axisymmetry. The domain is 2×4 and 300×300 nodes are used. A fixed non-uniform structured grid is employed. The smallest mesh size is 0.0003×0.001 near the contact region, where higher resolution is needed. As mentioned by Gondret *et al.* (2002), for moderate Reynolds number, the lateral walls have negligible effects on the collision process. The authors compared the results for the largest (10 cm) and smallest (0.6 cm) tanks and did not observe any difference within the accuracy of their measurements. We also carried out domain-independence tests and obtained the same results. First, the effect of surface roughness on the effective coefficient of restitution will be discussed. For this purpose, the sphere is released 0.6 cm above

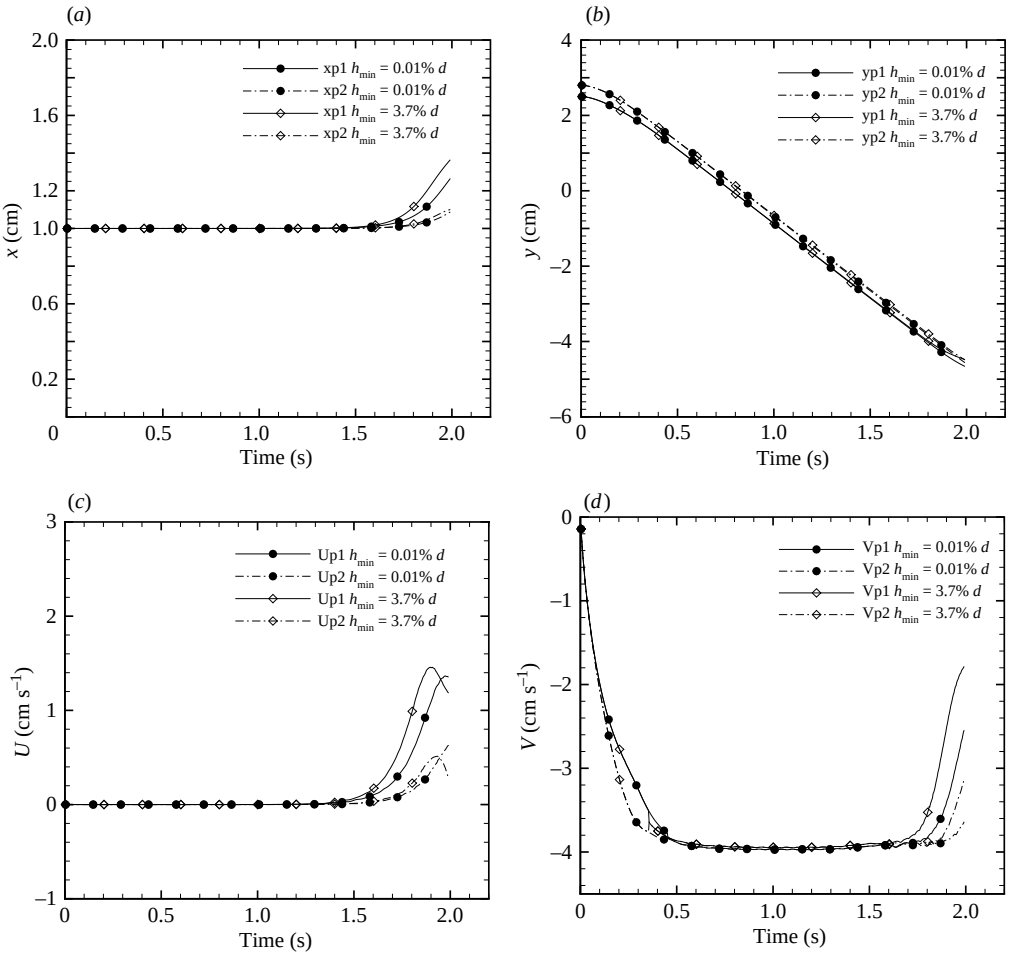

FIGURE 10. Sedimentation of two circular particles. In the first case (•), the roughness height is 0.01% of the particle diameter and in the second case (◇), it is 3.7% of the particle diameter. The mesh size is 0.014 and the time step is 0.0035. (*a*) Horizontal position, (*b*) Vertical position, (*c*) u velocity, (*d*) v velocity.

the wall. The distance h from the bottom of the sphere to the wall and the particle velocity are shown in figure 12. The Reynolds number based on the approach velocity of the sphere and the wall is 62.7 and the impact Stokes number is 58. As can be seen, rebound trajectories are non-parabolic since the velocity decreases nonlinearly with time.

A jump in velocity occurs when the particle surfaces come into contact (the surface itself for smooth particles, the surface bumps for rough particles). At this time, no liquid is present between the two surfaces and consequently the velocity jumps to $V^{t_c^+} = -e_{dc} V^{t_c^-}$, where e_{dc} is the dry coefficient of restitution. Subsequently, the particle moves away from the wall and liquid re-enters the gap. A marked decrease in the particle velocity is due to the large viscous dissipation. Because of this marked reduction in particle velocity in a very small time, the experimentally measured coefficient of restitution depends on the resolution of the device used to capture the particle velocity. The scatter in the experimental data could be due to the same fact

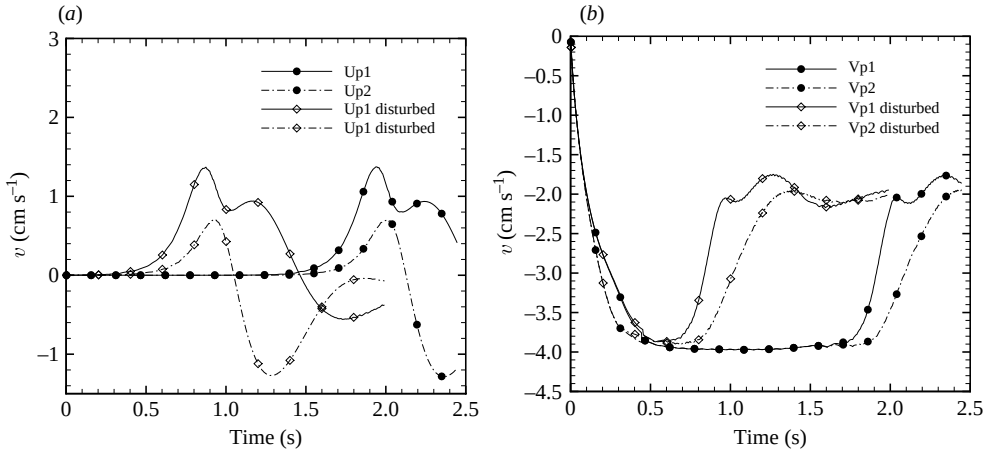

FIGURE 11. Sedimentation of two circular particles. In the first case (•), the particles are initially aligned at the centre of the channel and in the second case (◇), the upper particle is initially displaced to the right a distance of 0.5% of the particle diameter. The mesh size is 0.014 and the time step is 0.0017. (*a*) u velocity, (*d*) v velocity.

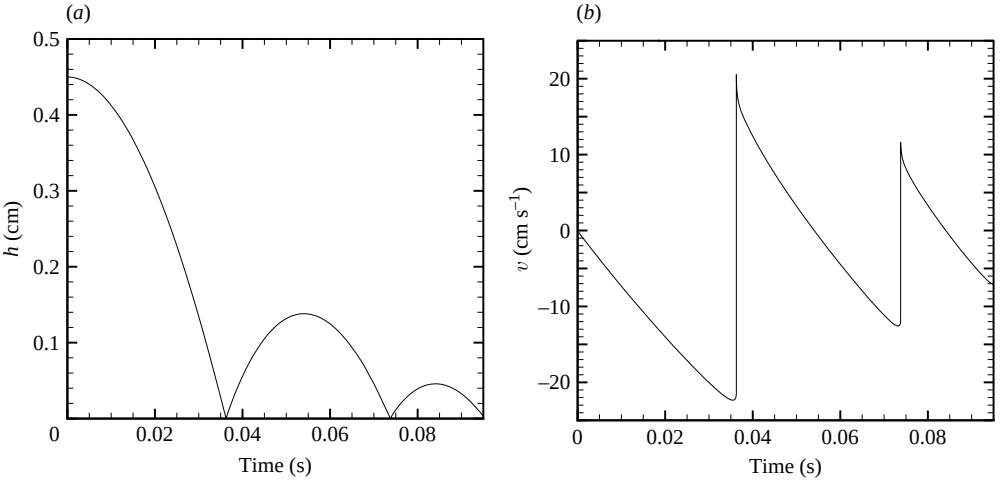

FIGURE 12. Sedimentation of a spherical particle and its collision with a wall. $Re = 63$, $St = 58$, $h_{\min} = 1.2\,\mu$m, and $e_{dc} = 0.97$. (*a*) Distance between particle surface and the wall, (*b*) Vertical velocity.

in addition to the roughness of the surfaces. As the sphere moves away from the wall and the gap widens, viscous dissipation decreases and the velocity varies more slowly. We have compared our numerical results with the experimental results by Gondret *et al.* (2002). In their work, the sphere motion is captured by a high speed video camera at 500 images per second. Thus, in order to compare the effective coefficient of restitution with their experimental results, the coefficient of restitution is defined as the velocity of the sphere at $t_c + 0.001$s divided by the pre-collision velocity. One could ideally define the post collision velocity at the time of transition from rapid velocity change to slow velocity change. However, the period of rapidly changing velocity is too short to be measured experimentally. In addition, we observed a 5 % decrease in the velocity before rebound. Joseph *et al.* (2001) observed this phenomenon whereas

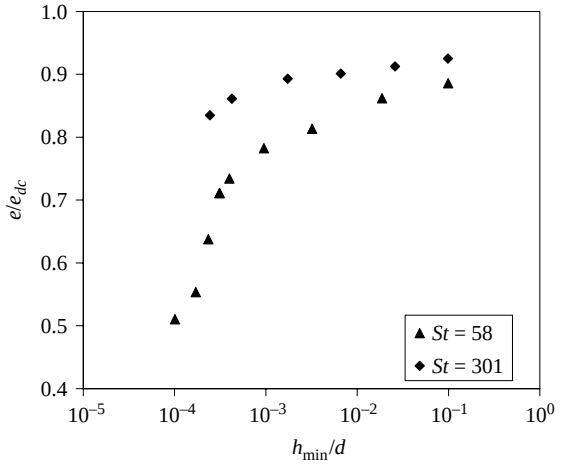

FIGURE 13. Coefficient of restitution versus surface roughness.

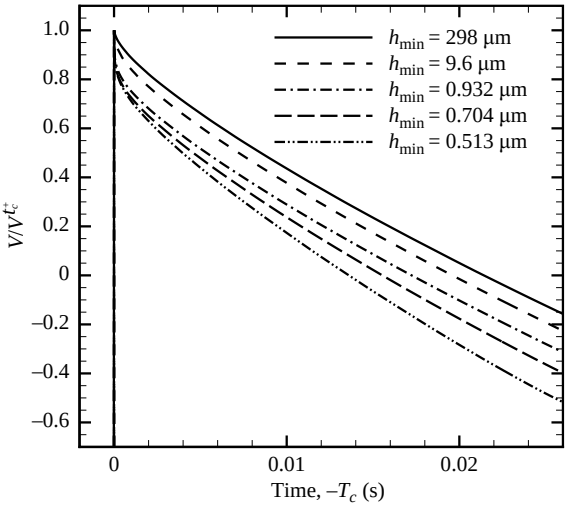

FIGURE 14. Velocity of the particle normalized by $V^{t_c^+}$ as function of time. $St = 58$ and $e_{dc} = 0.97$.

Gondret *et al.* did not, perhaps due to the fact that this decrease occurs in 0.8 ms but their resolution is 500 images per second. Figure 13 shows the effective coefficient of restitution versus surface roughness for the cases with Stokes number of 58 and 301. As can be observed, the amount of rebound increases for higher surface roughness. For $h_{\min} = 0.302\,\mu$m and $St = 58$, the effective coefficient of restitution decreases to 0.5. In figure 14, the normalized post-collision particle velocity versus time after collision is presented for different roughness heights. In order to compare the effect of roughness on the velocity reduction in the gap between the particle and the wall, the velocity is normalized by $V^{t_c^+}$. It can be seen that the velocity decreases in a very short time and this is more markedly so for smoother spheres.

Davis *et al.* (2003) showed that the microscopic surface roughness generally lowers the effective viscosity of low-Reynolds-number suspensions, as they reduce viscous

dissipation due to near-contact lubrication stresses. Here, we observed that increasing surface roughness reduces viscous dissipation and increases the effective coefficient of restitution at intermediate Reynolds numbers.

The velocity profile in the gap for a case with impact Stokes number of 58 and $h_{\min} = 0.932\,\mu\text{m}$ is shown in figure 15. At 173 μs before collision, a parabolic-like velocity profile can be seen. As time elapses, the maximum velocity increases until the gap width is equal to $h_{\min}$, at which point the collision starts. At this time, a large jump is seen in the velocity profile and particle velocity. Beyond this time, the maximum velocity in the gap decreases as the particle moves away from the wall and the velocity profile develops toward the parabolic-like shape in the opposite direction. Figure 16 shows the streamlines a short time before (*a*) and a short time after (*b*) collision. The streamlines far from the sphere are similar in (*a*) and (*b*) due to the fluid inertia. However, close to the sphere, the flow direction is changed after the collision process. The flow direction close to the wall is changed also due to the pressure gradient, which is generated by upward motion of the sphere. The difference between the velocity profiles before and after the collision process in the gap between the sphere and the wall is shown in figure 17. It can be observed that it is very close to the potential flow solution due to the impulsive motion of a sphere (jump in the velocity). Thin boundary layers are seen close to the wall and the sphere. The streamlines are shown in figure 18, which agrees with the potential solution given by Milne-Thomson (1968). As explained in the Introduction, integrating the Navier–Stokes equation from t_c^- to t_c^+, one obtains equation (1.1). It has been shown that for an impulsive motion starting from rest, $\boldsymbol{u}(t_c^+)$ is irrotational (Milne-Thomson 1968). For an impulsive motion which is not initially quiescent, integrating the vorticity equation from t_c^- to t_c^+ results in a vorticity jump equal to zero. Hence, the velocity jump $(\boldsymbol{u}(t_c^+) - \boldsymbol{u}(t_c^-))$ is irrotational. On the other hand, (1.1) clearly shows that the velocity jump is a gradient of a function. Despite the presence of the wall, where additional vorticity is produced, the velocity difference $(\boldsymbol{u}(t_c^+) - \boldsymbol{u}(t_c^-))$ is irrotational due to the fact that it takes a while for the vorticity generated at the wall to be diffused. Using this irrotational flow the added mass can be calculated.

Figure 19 compares the results using our numerical method with the experimental results by Gondret *et al.* For larger Stokes number, higher rebound is observed, as expected. It can be seen that the coefficient of restitution we obtain numerically is in a very good agreement with the experimental measurements. A general description of rebound is proposed by Legendre *et al.* (2006) for both solid particles and liquid drops. They obtained a correlation between the global coefficient of restitution ε and the Stokes number that incorporates the inertia of the particle (added mass included) and the viscous force exerted on the particle during the drainage of the liquid film between the particle and the wall. Here ε is defined as a ratio of the velocity of particle after collision $V^{t_c^+}$ to the velocity V_∞ before it decreases due to the interaction with the wall:

$$\varepsilon = \frac{V^{t_c^+}}{V_\infty}. \tag{5.1}$$

The Stokes number St^* including added mass is defined as follows:

$$St^* = \frac{(\rho_P + C_{M\infty}\rho_f)V_\infty d}{9\mu}, \tag{5.2}$$

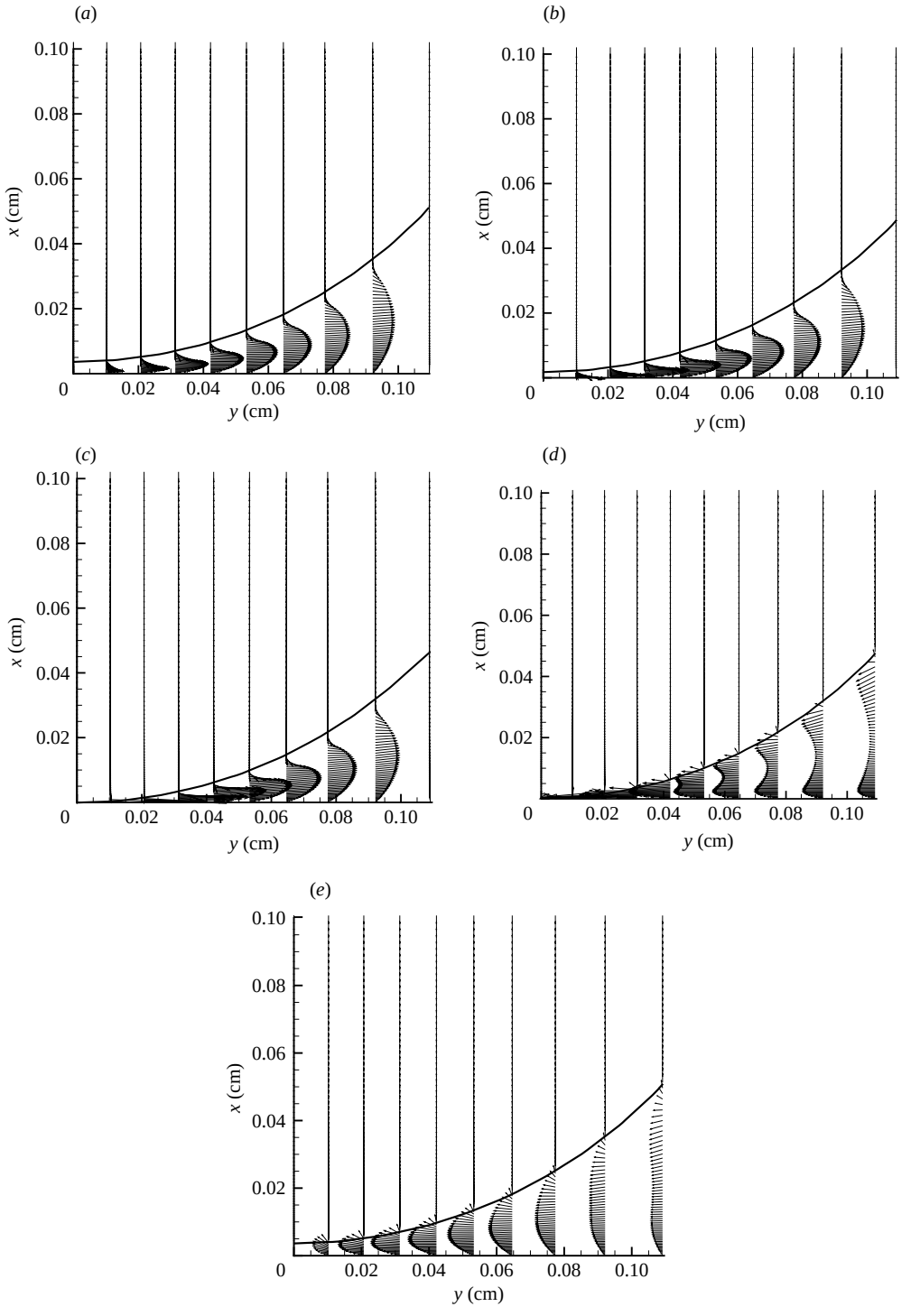

FIGURE 15. Velocity vectors in the gap between a sphere and wall during the collision process. $St = 58$, $h_{\min} = 0.932\,\mu\text{m}$, and $e_{dc} = 0.97$. (*a*) Time $- t_c = -173\,\mu\text{s}$, (*b*) time $- t_c = -81\,\mu\text{s}$, (*c*) time $- t_c = -1.1\,\mu\text{s}$, (*d*) time $- t_c = 9.9\,\mu\text{s}$, (*e*) time $- t_c = 215\,\mu\text{s}$.

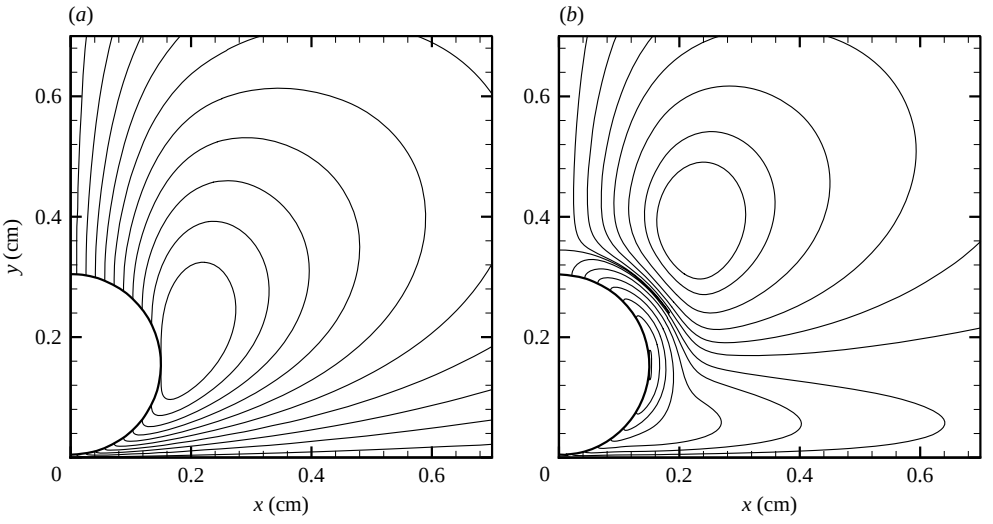

FIGURE 16. The streamlines before and after the collision process. $St = 58$, $h_{\min} = 0.932\,\mu\text{m}$, and $e_{dc} = 0.97$. (*a*) Time $- t_c = -173\,\mu\text{s}$, (*b*) time $- t_c = 215\,\mu\text{s}$.

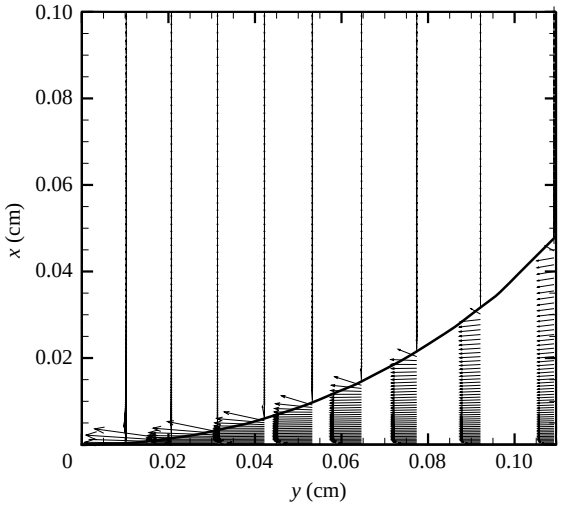

FIGURE 17. The difference between the velocity profiles before and after collision in the gap between the sphere and the wall. $St = 58$, $h_{\min} = 0.932\,\mu\text{m}$, and $e_{dc} = 0.97$.

where $C_{M\infty} = 1/2$ is the added mass coefficient. They showed that the coefficient of restitution can be correlated as

$$\epsilon = \epsilon_{dc} \exp\left(-\frac{\beta}{St^*}\right), \tag{5.3}$$

where $\beta = 35$ fits the general trend followed by the experimental data. Figure 20 shows the curve obtained using equation (5.3), experimental results, and our numerical results. Furthermore, we find that the effect of roughness on the coefficient of restitution decreases as the Stokes number increases, as shown in figure 21. There is no quantitative experimental observation on the effect of surface roughness on the effective coefficient of restitution, which could be due to the fact that, as Joseph

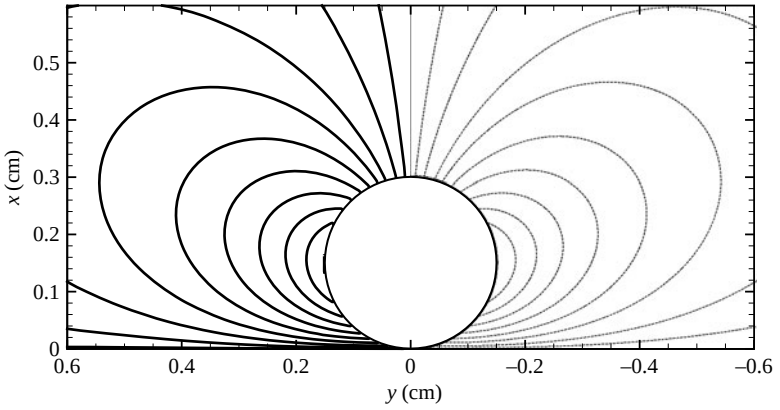

FIGURE 18. Streamlines for the difference between the velocities before and after collision (left half) and potential flow solution of a sphere approaching a wall (Milne-Thomson 1968) (right half). $St = 58$, $h_{\min} = 0.932\,\mu\text{m}$, and $e_{dc} = 0.97$.

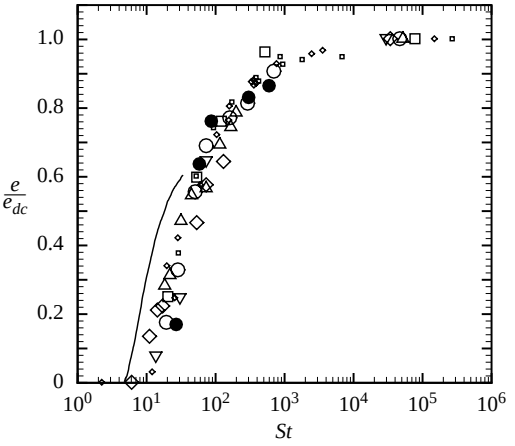

FIGURE 19. Coefficient of restitution normalized by that for dry collision as a function of St. Present results (●), where $h_{\min} = 0.7\,\mu\text{m}$. Experimental measurements for different materials by Gondret *et al.* (2002): tungsten carbide (□), steel (◇), glass (○), Teflon (□), Derlin (△), polyurethane (▽), and Nylon (◇). Roughness in these experimental cases is less than 1 μm. Lubrication theory of Davis *et al.* (1986) (—).

et al. (2001) indicated, the characteristic variance observed in the measurement of the coefficient of restitution is of the order of the experimental uncertainty for smooth particles and considerably larger for the rougher particles. In the cases studied in this section, the roughness height is at least an order of magnitude larger than the elasticity length scale. Thus the deformation of particles is neglected.

It has been shown theoretically and numerically that the added mass for a given particle is unaltered by finite-Reynolds-number effects and that the contribution to the total force acting on the particle that depends on the instantaneous value of the acceleration is identical to that predicted by irrotational theory (Legendre *et al.* 2003). Kushch *et al.* (2002) calculated the added mass coefficient for a bubble in potential flow by evaluating the impulse using a potential function. For a solid particle moving

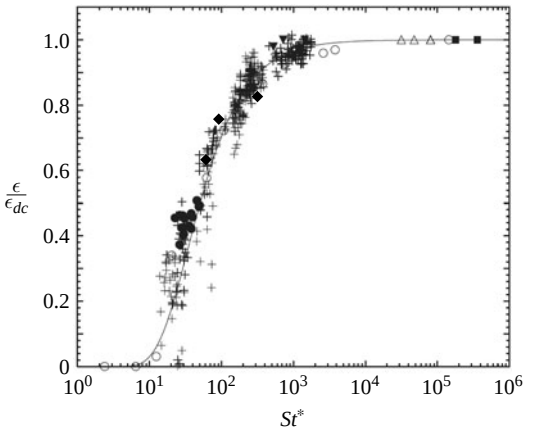

FIGURE 20. Global coefficient of restitution normalized by that for a dry collision as a function of St^*. Present results (◆) where $h_{\min} = 0.7\,\mu\text{m}$; toluene drops in water by Legendre, Daniel & Guiraud (2005) (●); liquid drop in air by Richard & Quéré (2000) (▼); spherical balloon filled with a mixture of water and glycerol by Richard & Quéré (2000) (■); solid spheres by Joseph *et al.* (2001) (+); solid sphere by Gondret *et al.* (2002) (○); solid sphere by Foerster *et al.* (1994) (△); correlation given by Legendre *et al.* (2006) (−).

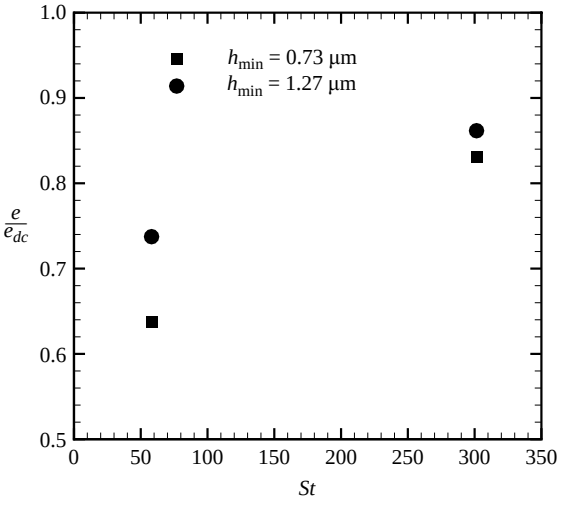

FIGURE 21. Coefficient of restitution normalized by that for a dry collision as a function of St for different roughness heights.

normal to the wall, the added mass coefficient is equal to

$$C_M = \frac{1}{2}\left\{1 + \frac{3}{8}\left(\frac{a}{a+h}\right)^3\right\}$$

up to order $(h/a)^3$, where a is the sphere radius (Milne-Thomson 1968). One can use viscous potential flow theory for a sphere moving normal to a wall (Ardekani, Rangel & Joseph 2007) to calculate the contribution of the force applied to the particle which is proportional to the particle acceleration. The potential flow solution for this problem can be obtained using the image of a doublet source in a sphere and

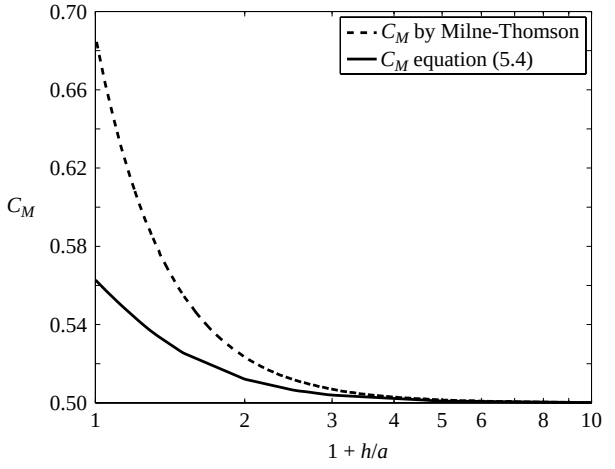

FIGURE 22. Added mass coefficient for a sphere moving normal to a wall.

is given as a series. The added mass coefficient is plotted in figure 22 and is compared with C_M given earlier. The solid curve shown in figure 22 can be described as

$$C_M = \frac{1}{2}\left\{1 + \frac{1.591}{(1.917 + h/a)^{3.887}}\right\}. \tag{5.4}$$

For $Re \ll 1$, the particle equation of motion can be written as

$$(C_M m_f + m_p)\frac{\mathrm{d}U}{\mathrm{d}t} = (m_f - m_p)g - 6\pi\mu a\lambda U + F_h. \tag{5.5}$$

For a spherical particle moving normal to a wall, λ has been calculated by several researchers using bispherical coordinates as

$$\lambda = \frac{4}{3}\sinh\alpha \sum_{n=1}^{\infty} \frac{n(n+1)}{(2n-1)(2n+3)}\left[\frac{2\sinh(2n+1)\alpha + (2n+1)\sinh 2\alpha}{4\sinh^2(n+\frac{1}{2})\alpha - (2n+1)^2\sinh^2\alpha} - 1\right] \tag{5.6}$$

(Brenner 1961), where $\cosh\alpha = h/a$. The history term F_h is known for an isolated sphere in Stokes flow. It has been shown by Ardekani & Rangel (2006) that the history force for two spheres moving side by side or in tandem is larger than the history force of an isolated sphere. Similarly, the presence of the wall will affect the history force. However, the quantitative form of the expression for the history force including wall effects is not known. Considering the drag force applied to the particle, the added mass calculated from equation (5.4), and a velocity jump upon contact at $h = h_{\min}$, the effective coefficient of restitution can be calculated. The results are shown in figure 23(*a*). The coefficient of restitution has a logarithmic dependence on surface roughness, as has been shown by Sundararajakumar & Koch (1996) and Sangani *et al.* (1996). For Stokes numbers larger than 30, as shown in figure 23(*b*), the slope of the coefficient of restitution versus the logarithm of $h_{\min}$ is inversely proportional to St. Numerical data shows a similar trend for $h_{\min} > 2\,\mu\mathrm{m}$. However, their intersects are smaller than those from the theoretical data. This is due to the fact that the history term is neglected. It has been shown that the coefficient of restitution calculated this way does not depend on the Reynolds number (Davis *et al.* 1986). Numerically, we calculated the effective coefficient of restitution for $St = 301$ and $h_{\min} = 77\,\mu\mathrm{m}$ and two different Reynolds numbers of 162 and 35. The coefficient of restitution at $Re = 35$

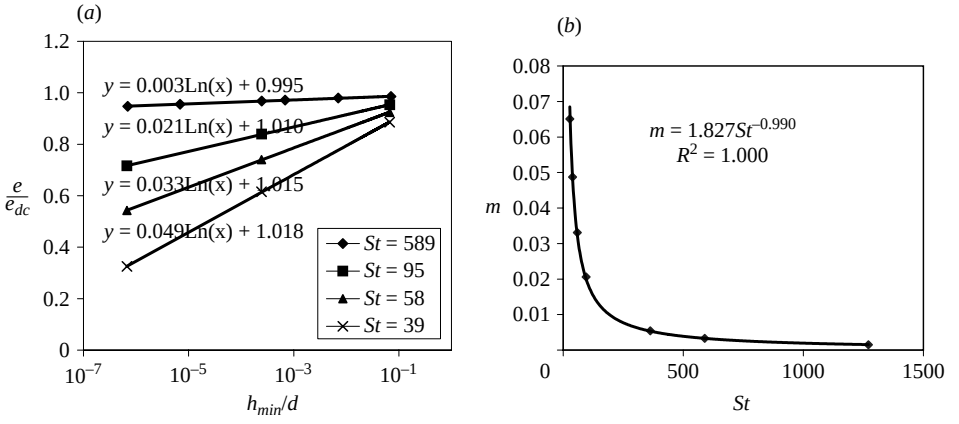

FIGURE 23. Effective coefficient of restitution for a spherical particle colliding with a wall at $Re \ll 1$.

is only 4.5 % higher than the one at $Re = 162$. Thus, Re has a smaller effect on the effective coefficient of restitution compared to the Stokes number.

5.4. *Vortex dynamics of a sphere colliding onto a wall*

When a sphere moves towards a wall and stops upon making contact with it, a secondary vortex ring is generated from the wake vorticity. The evolution of vorticity for this problem is considered numerically by Thompson *et al.* (2006, 2007) and experimentally by Eames & Dalziel (2000). Thompson *et al.* (2007) observed that, at Reynolds numbers higher than about 1000, a non-axisymmetric instability develops, leading to rapid distortion of the ring system. Using linear stability and direct numerical simulation, they found that the non-axisymmetric instability is centrifugal in nature. In these studies, the sphere sticks to the wall after the collision. In the present work, we discuss the vortex dynamics associated with the collision of a sphere and a wall for non-zero coefficient of restitution when rebound occurs.

First, we compare our numerical results with experimental results by Eames & Dalziel (2000). In this case, a sphere is set into motion from a distance of $L = 7.5d$ above the wall and moves with constant velocity and a Reynolds number of 850. A non-uniform structured grid and a domain size of $10d \times 20d$ with 300×350 nodes are employed. Figure 24 shows the vorticity contours when the sphere, which is moving with constant velocity before the collision, sticks to the wall after collision. The left and right sides of each frame in the figure show the present numerical results and the experimental results by Eames & Dalziel (2000), respectively. This comparison shows very good agreement. In figure 24(a, b) the wake vorticity of the sphere approaching the wall can be observed. As the sphere stops, the wake vorticity moves towards the wall due to its inertia. The wake vortex threads over the sphere and generates a secondary vortex ring as seen in figure 24(c). This coherent structure, composed of the wake and secondary vortices, leaves the sphere and strikes the wall, as seen in figure 24(d). The secondary vortex is stretched by the wake vortex and becomes a sheet-like structure (figure 24e, f). Finally, the secondary vortex extends radially and breaks into two parts. One part is advected around the wake vortex while the second component remains trapped close to the point of contact between the sphere and the wall in figure 24(g).

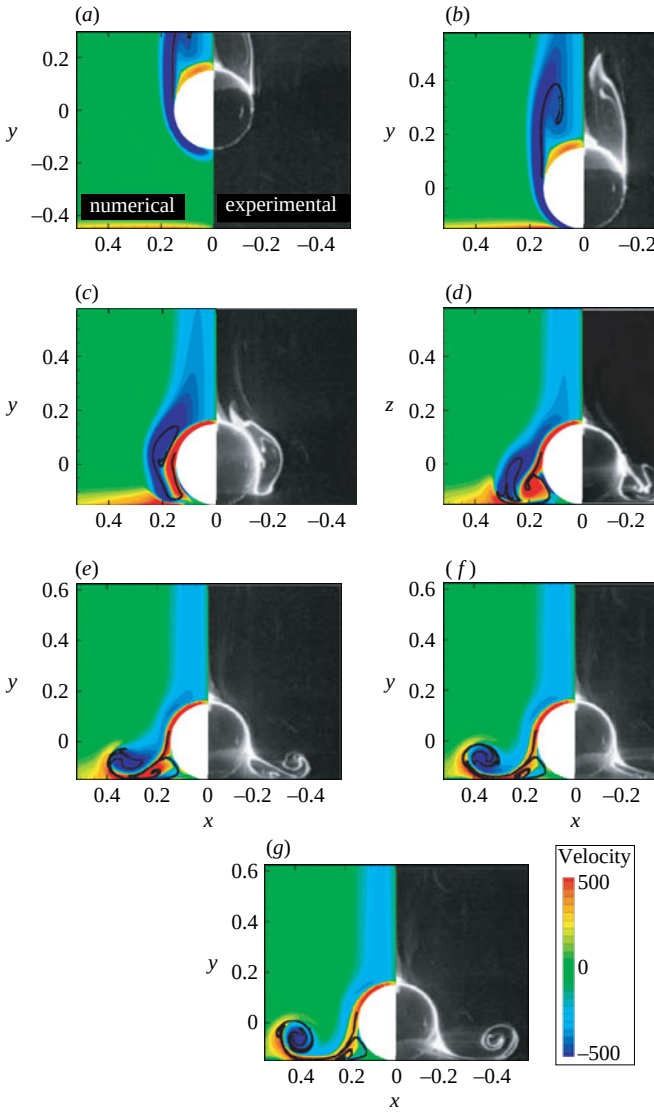

FIGURE 24. Collision of a sphere onto a wall. The left half and right half of each frame corresponds to the present numerical results and the experimental results by Eames & Dalziel (2000), respectively. $Re = 850$, $h_{\min} = 9.2\,\mu$m. The vorticity contours are shown and the black line is a streakline. $(a) -\tau'$, (b) 0, (c) τ', (d) $2\tau'$, (e) $3\tau'$, (f) $4\tau'$, (g) $5\tau'$ where $\tau' = D/U$.

The motion of a sphere falling under gravity is considered next. The sphere is released from a height of $L = 5d$ with a Reynolds number of 510 based on the initial velocity. The Reynolds number increases to 865 when the particle collides with the wall. The vorticity contours are shown in figure 25. The coefficient of restitution for a dry collision is zero in the left half and 0.5 in the right half of each frame of figure 25. In frame(a), both sides correspond to a time before collision and are the same. As time elapses (figure 25b), a secondary vortex ring is generated in both cases while the wake vortex is moving towards the wall due to its inertia. In the right half of figure 25(b), a secondary vortex is growing and becoming the wake vortex for

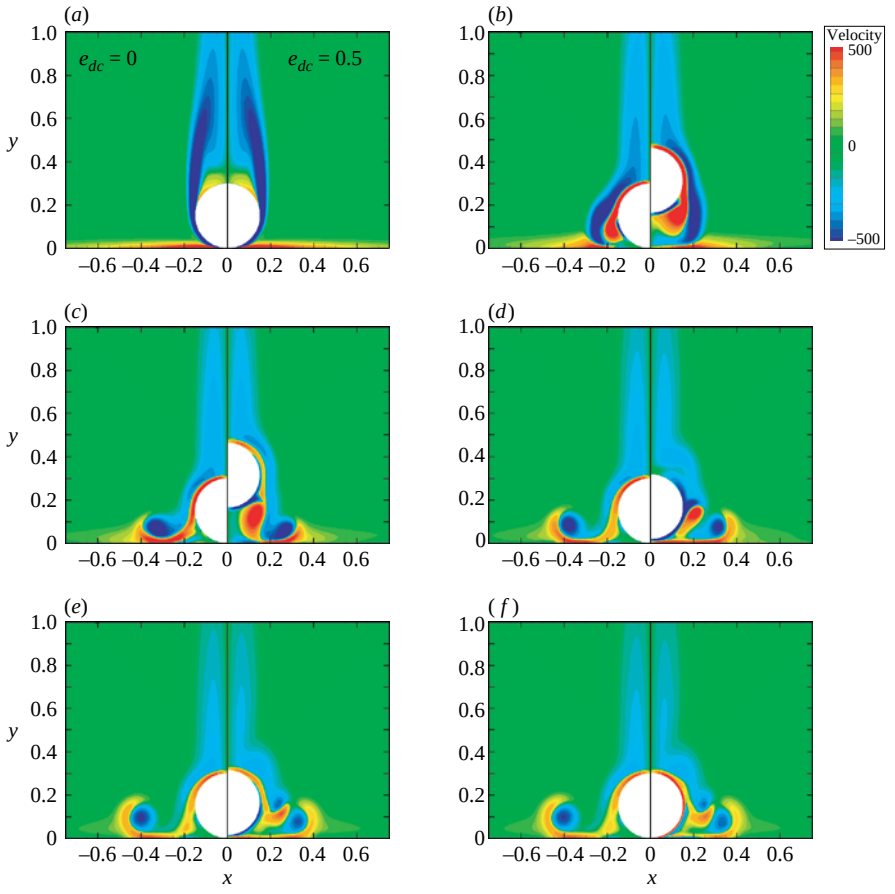

FIGURE 25. Collision of a sphere onto a wall. The coefficient of restitution for a dry collision is zero in the left half and 0.5 in the right half of each frame. Vorticity contours are shown. $Re = 865$, $h_{\min} = 9.8\,\mu\text{m}$, and $\tau' = \sqrt{d/g}$. (*a*) Before collision, (*b*) $0.76\tau'$, (*c*) $1.56\tau'$, (*d*) $2.36\tau'$, (*e*) $3.16\tau'$, (*f*) $3.39\tau'$.

the up-going sphere. A separated region on the sphere surface with vorticity of the same sign as the primary vortex is observed in both cases. In addition, a region with the opposite sign of the primary vorticity is generated in both cases at the wall. In the left half of the figure 25(*c*), a coherent structure leaves the sphere and extends radially, whereas in the right side of this frame, since the particle is moving downward, anti-clockwise vorticity spreads out below the sphere. The secondary vortex is divided into two portions, one above the sphere on the surface, while the larger portion of this secondary vortex remains between sphere and the wall. In figure 25(*d*), since the particle is moving downwards, the clockwise vorticity above the sphere is diffused while the anti-clockwise vorticity below the sphere grows. The coherent structure which has extended radially and the primary vortex far above the sphere are similar to the case without rebound. In of figure 25(*e*, *f*), the vortices have diffused and clockwise or anti-clockwise vorticity is observed around the sphere for upward and downward motion of the sphere, respectively.

Figure 26 shows a comparison between the cases of zero coefficient of restitution (left half of each frame) and dry coefficient of restitution equal to 1 (right half of each

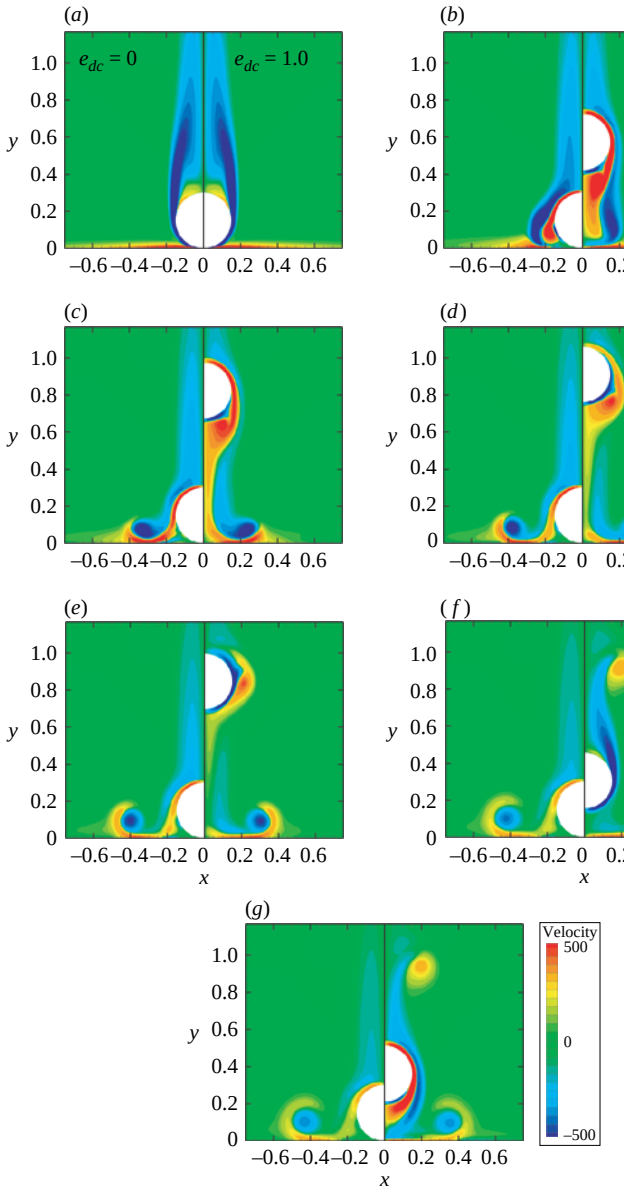

FIGURE 26. Collision of a sphere onto a wall. The coefficient of restitution for a dry collision is zero in the left half and 1.0 in the right half of each frame. Vorticity contours are shown. $Re = 865$, $h_{\min} = 9.8\,\mu$m, and $\tau' = \sqrt{d/g}$. (*a*) Before collision, (*b*) $0.76\tau'$, (*c*) $1.56\tau'$, (*d*) $2.36\tau'$, (*e*) $3.16\tau'$, (*f*) $4.76\tau'$, (*g*) $5.56\tau'$.

frame). Figures 26(*a*)–26(*c*) are similar to the corresponding frames of the previous case, except that now, the secondary vortex, which is the wake vortex during the upward motion of the sphere, is larger than the one observed at the same time in figure 25. In figure 26(*d*, *e*), the clockwise vorticity below the sphere moves above it due to the change in direction of the motion of the sphere. In figure 26(*f*) this clockwise vorticity which remained from the secondary vortex is advected from the sphere and deviates the wake vortex of the downward moving sphere. The coherent

structure near the wall is similar to that encountered for the case without rebound. In general, the vorticity field is stronger for larger dry coefficient of restitution due to the fact that less energy is dissipated during the collision process.

The correlation in equation (5.3) suggests that the inertia of the fluid only influences the coefficient of restitution through the added mass. This may be surprising given the rich vortex dynamics shown in this section. However, even though the inertia of the fluid significantly affects the flow field, it does not affect the effective coefficient of restitution which is measured on a much smaller time scale. This is in agreement with the fact that the Reynolds number has a small effect on the effective coefficient of restitution. It is noteworthy that the vortical structures that detach from the sphere as a result of the collision do not affect the rebound process. Results presented for the collision of a droplet on a wall in figure 20 indicate the same trend. One could argue that the entire process is dominated by the flow in the gap between the object and the wall.

6. Conclusions

In this paper, we describe a finite-volume distributed Lagrange multiplier algorithm to solve particulate flows with and without collisions. We show that our fluid–particle solver produces results which are in very good agreement with numerical studies of benchmark viscous flow problems. An efficient approach is introduced to simulate collision between particles. Instead of applying a repulsive force between particles, as was done by previous researchers, the contact force is calculated and its magnitude is the criterion which determines the end of the contact. An advantage of this method is that particles can touch and there is no need to choose a stiffness parameter *a priori*. Comparing our results for the bouncing motion of a solid sphere onto a solid plate in an ambient fluid for different Stokes numbers shows very good agreement with the results by Gondret *et al.* (2002). We also provide a new description and interpretation of the collision process in a viscous flow. Furthermore, it is shown that the effect of surface roughness on rebound decreases for higher Stokes numbers. The evolution of vorticity due to collision of a sphere with a wall and the effect of the coefficient of restitution are discussed.

We are grateful to Professor D. D. Joseph for valuable discussions.

REFERENCES

Ardekani, A. M. & Rangel, R. H. 2006 Unsteady motion of two solid spheres in Stokes flow. *Phys. Fluids* **18**, 103306.

Ardekani, A. M., Rangel, R. H. & Joseph, D. D. 2007 Motion of a sphere normal to a wall in a second-order fluid. *J. Fluid Mech.* **587**, 163–172.

Arp, A. P. & Mason, S. G. 1977 The kinetics of flowing dispersions: IX. Doublets of rigid spheres (experimental). *J. Colloid Interface Sci.* **61**, 44.

Barnocky, G. & Davis, R. H. 1989 The influence of pressure-dependent density and viscosity on the elastohydrodynamic collision and rebound of two spheres. *J. Fluid Mech.* **209**, 501–519.

Brady, J. F. & Bossis, G. 1988 Stokesian dynamics. *Annu. Rev. Fluid Mech.* **20**, 111–157.

Brenner, H. 1961 The slow motion of a sphere through a viscous fluid towards a plane surface. *Chem. Engng Sci.* **16**, 242.

Davis, R. H. 1987 Elastohydrodynamic collisions of particles. *PCH PhysicoChem. Hydrodyn.* **9**, 41–52.

Davis, R. H. 1992 Effect of surface roughness on a sphere sedimenting through a dilute suspension of neutrally buoyant spheres. *Phys. Fluids* A **4**, 2607–2619.

Davis, R. H., Serayssol, J. M. & Hinch, E. J. 1986 The elastohydrodynamic collision of two spheres. *J. Fluid Mech.* **163**, 479.

Davis, R. H., Zhao, Y., Galvin, K. P. & Wilson, H. J. 2003 Solid–solid contacts due to surface roughness and their effects on suspension behaviour. *Phil. Trans. R. Soc. Lond.* A **361**, 871–894.

Eames, I. & Dalziel, S. B. 2000 Dust resuspension by the flow around an impacting sphere. *J. Fluid Mech.* **403**, 305.

Ekiel-Jezewska, M. L., Feuillebois, F., Lecoq, N., Masmoudi, K., Anthore, R., Bostel, F. & Wajnryb, E. 1999 Hydrodynamic interactions between two spheres at contact. *Phys. Rev.* E **59**, 3182.

Ekiel-Jezewska, M. L., Lecoq, N., Anthore, R., Bostel, F. & Feuillebois, F. 2002 Rotation due to hydrodynamic interactions between two spheres in contact. *Phys. Rev.* E **66**.

Feng, J., Hu, H. H. & Joseph, D. D. 1994 Direct simulation of initial value problems for the motion of solid bodies in a Newtonian fluid. Part 1. Sedimentation. *J. Fluid. Mech.* **261**, 95–134.

Foerster, S. F., Lounge, M. Y., Chang, H. & Allia, K. 1994 Measurements of the collision properties of small spheres. *Phys. Fluids* **3**, 1108.

Glowinski, R., Pan, T. W., Hesla, T. I. & Joseph, D. D. 1999 A distributed Lagrange multiplier fictitious domain method for particulate flows. *Intl J. Multiphase Flow* **25**, 755–794.

Glowinski, R., Pan, T. W. & Periaux, J. 1998 distributed Lagrange multiplier method for incompressible viscous flow around moving rigid bodies. *Comput. Methods Appl. Mech. Engng* **151**, 181–194.

Gondret, P., Hallouin, E., Lance, M. & Petit, L. 1999 Experiments on the motion of a solid sphere toward a wall: From viscous dissipation to elastohydrodynamic bouncing. *Phys. Fluids* **11**, 2803–2805.

Gondret, P., Lance, M. & Petit, L. 2002 Bouncing motion of spherical particles in fluids. *Phys. Fluids* **14**, 643–652.

Hu, H. H., Patankar, N. A. & Zhu, M. Y. 2001 Direct numerical simulations of fluid–solid systems using the arbitrary Lagrangian–Eulerian technique. *J. Comput. Phys.* **169**, 427–462.

Joseph, G. G. & Hunt, M. L. 2004 Oblique particle-wall collisions in a liquid. *J. Fluid Mech.* **510**, 71–93.

Joseph, G. G., Zenit, R., Hunt, M. L. & Rosenwinkel, A. M. 2001 Particle-wall collisions in a viscous fluid. *J. Fluid Mech.* **433**, 329–346.

Kushch, V. I., Sangani, A. S., Spelt, P. D. M. & Koch, D. L. 2002 Finite-Weber-number motion of bubbles through a nearly inviscid liquid. *J. Fluid Mech.* **460**, 241–280.

Ladd, A. J. C. 1994*a* Numerical simulation of particulate suspensions via a discretized Boltzmann equation. Part 1. Theoretical foundation. *J. Fluid Mech.* **271**, 271–309.

Ladd, A. J. C. 1994*b* Numerical simulation of particulate suspensions via a discretized Boltzmann equation. Part 2. Numerical results. *J. Fluid Mech.* **271**, 311–339.

Legendre, D., Daniel, C. & Guiraud, P. 2005 Experimental study of a drop bouncing on a wall in a liquid. *Phys. Fluids* **17**, 1–13.

Legendre, D., Magnaudet, J. & Mougin, G. 2003 Hydrodynamic interactions between two spherical bubbles rising side by side in a viscous liquid. *J. Fluid Mech.* **497**, 133–166.

Legendre, D., Zenit, R., Daniel, C. & Guiraud, P. 2006 A note on the modelling of the bouncing of spherical drops or solid spheres on a wall in viscous fluid. *Chem. Engng Sci.* **61**, 3543–3549.

Lin, J. Z., Wang, Y. L. & Olsen, J. A. 2004 Sedimentation of rigid cylindrical particles with mechanical contacts. *Chin. Phys. Lett.* **22**, 628–631.

Milne-Thomson, L. M. 1968 *Theoretical Hydrodynamics*. Dover.

Patankar, N. A. 2001 A formulation for fast computations of rigid particulate flows. *Center for Turbulence Res., Annu. Res. Briefs* 185–196.

Patankar, N. A., Singh, P., Joseph, D. D., Glowinski, R. & Pan, T. W. 2000 A new formulation of the distributed Lagrange multiplier/fictitious domain method for particulate flows. *Intl J. Multiphase Flow* **26**, 1509–1524.

Patankar, S. V. 1980 *Numerical Heat Transfer and Fluid Flow*. McGraw-Hill.

Richard, D. & Quéré, D. 2000 Bouncing water drops. *Europhys. Letters* **50**, 769–775.

Sangani, A. S. & Mo, G. 1994 Inclusion of lubrication forces in dynamic simulations. *Phys. Fluids* **6**, 1653.

Sangani, A. S., Mo, G. B., Tsao, H. K. & Koch, D. L. 1996 Simple shear flows of dense gas-solid suspensions at finite Stokes numbers. *J. Fluid Mech.* **313**, 309.

Sharma, N., Chen, Y. & Patankar, N. A. 2005 A distributed Lagrange multiplier based computational method for the simulation of particulate-Stokes flow. *Comput. Methods Appl. Mech. Engng* **194**, 4716–4730.

Sharma, N. & Patankar, N. A. 2005 A fast computation technique for direct numerical simulation of rigid particulate flows. *J. Comput. Phys.* **205**, 439–457.

Singh, P., Hesla, T. I. & Joseph, D. D. 2003 Distributed Lagrange multiplier method for particulate flows with collisions. *Intl J. Multiphase Flow* **29**, 495–509.

Singh, P., Joseph, D. D., Hesla, T. I., Glowinski, R. & Pan, T. W. 2000 Direct numerical simulation of viscoelastic particulate flows. *J. Non-Newtonian Fluid Mech.* **91**, 165–188.

Smart, J. R. & Leighton, D. T. 1989 Measurement of the hydrodynamic surface-roughness of noncolloidal spheres. *Phys. Fluids* **1**, 52–60.

Sundararajakumar, R. R. & Koch, D. L. 1996 Non-continuum lubrication flows between particles colliding in a gas. *J. Fluid Mech.* **313**, 283.

Thompson, M. C., Hourigan, K., Cheung, A. & Leweke, T. 2006 Hydrodynamics of a particle impact on a wall. *Appl. Math. Modelling* **30**, 1356.

Thompson, M. C., Leweke, T. & Hourigan, K. 2007 Sphere-wall collisions: Vortex dynamics and stability. *J. Fluid Mech.* **575**, 121.

Tsao, H. K. & Koch, D. L. 1994 Collisions of slightly deformable, high Reynolds number bubbles with short range repulsive forces. *Phys. Fluids* **6**, 2591–2605.

Zeng, S., Kerns, E. T. & Davis, R. H. 1996 The nature of particle contact in sedimentation. *Phys. Fluids* **8**, 1389.

Zhang, J., Fan, L. S., Zhu, C., Pfeffer, R. & Qi, D. 1999 Dynamic behavior of collision of elastic spheres in viscous fluids. *Powder Tech.* **106**, 98–109.